HIGH FREQUENCY OPTICAL RECEIVERS

Cornell University

Jinwook Burm, Kerry Litvin, Lester F. Eastman,
Michael Leary, and Joseph Ballantyne

DTIC
S ELECTE D
SEP 2 6 1995
G

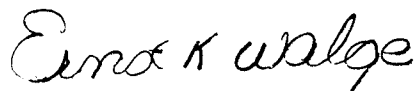| Accesion For		
NTIS CRA&I		☒
DTIC TAB		☐
Unannounced		☐
Justification		
By		
Distribution /		
Availability Codes		
Dist	Avail and / or Special	
A-1		

19950922 034

Rome Laboratory
Air Force Materiel Command
Griffiss Air Force Base, New York

This report has been reviewed by the Rome Laboratory Public Affairs Office (PA) and is releasable to the National Technical Information Service (NTIS). At NTIS it will be releasable to the general public, including foreign nations.

RL-TR-95-105 has been reviewed and is approved for publication.

APPROVED: *Ernst K Walge*

ERNST K. WALGE
Project Engineer

FOR THE COMMANDER: *Donald W. Hanson*

DONALD W. HANSON
Director of Surveillance & Photonics

REPORT DOCUMENTATION PAGE

Public reporting burden for this collection of information is estimated to average 1 hour per response, including the time for reviewing instructions, searching existing data sources, gathering and maintaining the data needed, and completing and reviewing the collection of information. Send comments regarding this burden estimate or any other aspect of this collection of information, including suggestions for reducing this burden, to Washington Headquarters Services, Directorate for Information Operations and Reports, 1215 Jefferson Davis Highway, Suite 1204, Arlington, VA 22202-4302, and to the Office of Management and Budget, Paperwork Reduction Project (0704-0188), Washington, DC 20503.

1. AGENCY USE ONLY (Leave Blank)	2. REPORT DATE June 1995	3. REPORT TYPE AND DATES COVERED Final Jul 91 – Apr 94

4. TITLE AND SUBTITLE

HIGH FREQUENCY OPTICAL RECEIVERS

6. AUTHOR(S)

Jinwook Burm, Kerry Litvin, Lester F. Eastman,
Michael Leary, and Joseph Ballantyne

5. FUNDING NUMBERS

C – F30602-91-C-0063
PE – 62702F
PR – 4519
TA – 21
WU – 92

7. PERFORMING ORGANIZATION NAME(S) AND ADDRESS(ES)

Cornell University
Office of Sponsored Programs
120 Day Hall
Ithaca NY 14853

8. PERFORMING ORGANIZATION REPORT NUMBER

N/A

9. SPONSORING/MONITORING AGENCY NAME(S) AND ADDRESS(ES)

Rome Laboratory (OCPC)
25 Electronic Pky
Griffiss AFB NY 13441-4515

10. SPONSORING/MONITORING AGENCY REPORT NUMBER

RL-TR-95-105

11. SUPPLEMENTARY NOTES

Rome Laboratory Project Engineer: Ernst K. Walge/OCPC/(315) 330-3147

12a. DISTRIBUTION/AVAILABILITY STATEMENT

Approved for public release; distribution unlimited.

12b. DISTRIBUTION CODE

13. ABSTRACT (Maximum 200 words)

A 44 GHz optical receiver was designed and fabricated that integrated a photodetector and transistors. Photodetector layers, designed for absorption of 770 nm light, contained an AlGaAs cap layer to prevent any surface recombination of carriers; a thin GaAs absorption layer (312 nm) used to achieve high frequency response (greater than 40 GHz) through high electric field and soft carrier path; and Bragg reflector layers, to reflect unabsorbed light back into the absorption region. The whole detector layer was designed to maximize the optical signal absorption.

14. SUBJECT TERMS Optical receivers, Photodetectors, Transistors	15. NUMBER OF PAGES 52
	16. PRICE CODE

17. SECURITY CLASSIFICATION OF REPORT UNCLASSIFIED	18. SECURITY CLASSIFICATION OF THIS PAGE UNCLASSIFIED	19. SECURITY CLASSIFICATION OF ABSTRACT UNCLASSIFIED	20. LIMITATION OF ABSTRACT UL

Table of Contents

Final Report on
Contract No. F30602-91-C-0063

High Frequency Optical Receivers
May 1, 1991 - April 30, 1994

Introduction

This contract covered two tasks. The final report will cover Section I - Optical Receiver Circuit Operating at 44 GHz and Section II - Waveguide Metal-Semiconductor - Metal Photodetectors for 44 GHz Integrated Preamplifier. Appendix A includes all papers and publications covered by both sections of this report.

I . Optical Receiver Circuit Operating at 44GHz -
Jinwook Burm, Kerry I. Litvin, and Lester F. Eastman

Abstract

We designed and fabricated 44GHz optical receivers integrating a photodetector and transistors. The photodetector layers, designed for the absorption of 770nm light, contained a AlGaAs cap layer, to prevent any surface recombination of carriers, a thin GaAs absorption layer (312nm), to achieve high frequency response (>40GHz) through high electric field and short carrier path, and Bragg reflector layers, to reflect unabsorbed light back into the absorption region. The whole detector layer was designed to maximize the optical signal absorption. Using this layer structure, we could achieve high frequency response without the cost of low quantum efficiency. The fabricated MSM interdigitated photodetector with $2\mu m$ gap on this detector layer showed the internal quantum efficiency of 82% at 5V bias and of close to 94% at 10V bias. The measured optical dynamic range of the MSM photodetectors were in excess of 33dB. The problems of long time response tail and low frequency gain, due to the surface exposure of the GaAs absorption layer, has been solved by etching the cap layer less and deposited metal fingers on AlGaAs cap layer. We also introduced a circular-aperture photodetectors to increase frequency response for a given detection area. The optimization of the MSM photodetector showed there exists a optimum number of fingers to maximize the frequency response regardless of the size of detectors, which is 33 for circular-aperture detectors and 29 for square-aperture detectors.

As post-detection amplifiers, pseudomorphic $In_{0.2}Ga_{0.8}As$ channel MODFET's were employed. With $0.12\mu m$ long gates, we could achieve 110GHz of f_t and 60GHz of f_{max}. For the optical receiver circuit, DC bias line with -0.13dB insertion loss was developed. By using coplanar waveguide matching, a optical receiver circuit with single stage amplifier showed 5.7dB overall gain at 44GHz.

I. Introduction

Metal-Semiconductor-Metal (MSM) photodetectors have shown great promises for optoelectronic integrated circuit applications because of their high frequency response and simple planar structure. Recently researchers have demonstrated MSM detectors with measured bandwidths greater than 350GHz [1], [2]. In addition to its superior frequency response, a MSM photodetector has an advantage of planar structure, which makes MSM photodetectors an ideal choice for optoelectronic circuits.

For photodetectors in optical receiver circuits, high quantum efficiency as well as fast frequency response are required. To achieve high bandwidth for a MSM detector, a general rule is to decrease the spacing between the fingers and the thickness of the absorption layer to decrease the carrier transit time. In addition, small size detectors yielding small capacitance are better for the high bandwidth. However decreasing the absorption layer thickness and having the small detection area hinder the high sensitivity. Achieving high sensitivity through high quantum efficiency for a MSM photodetector is especially difficult because of the metal fingers, electrodes to collect the optically generated carriers, blocking the incident light. To overcome this difficulty we employ the Bragg reflector layers beneath the absorption layer and impedance matching cap to ensure the maximum absorption of the incident light possible.

Making high speed optical receivers accompanies some of the considerations for better performance. The photodetector in the circuit must respond faster than desired receiver speed, and must be sensitive enough to generate ample signal, at the same time. Amplifiers are also required to provide enough gain without introducing too much noise. The impedance of each element in the circuit must be matched properly to maximize the transmission of signals. DC bias lines need to be connected suitably not to interfere the signal flows. In this final report of optical receiver circuits operable at 44GHz with MSM photodetectors, we will present the improvements and results made to meet the above considerations.

II. Layer Design and Growth

The layers for the optical receiver circuits were grown using Varian Gen II MBE machine. On GaAs substrate 16 1/2 stacks of quarter wavelength Bragg reflector layers alternating $Al_{0.3}Ga_{0.7}As$ and $Al_{0.9}Ga_{0.1}As$ layers were grown. These layers are for reflecting unabsorbed light back into GaAs absorption layer for the additional absorption. On the top of the Bragg reflector layer, thin GaAs absorption layer, 312nm, and $Al_{0.3}Ga_{0.7}As$ cap layer were added. $Al_{0.3}Ga_{0.7}As$ cap layer is important to confine the carriers within the absorption region without surface recombination and to match the characteristic impedance of the air to that of the detector layer. The MODFET layers grown on the top of the detector layers contain pseudomorphic $In_{0.2}Ga_{0.8}As$ channel for better frequency characteristics (Fig. 1).
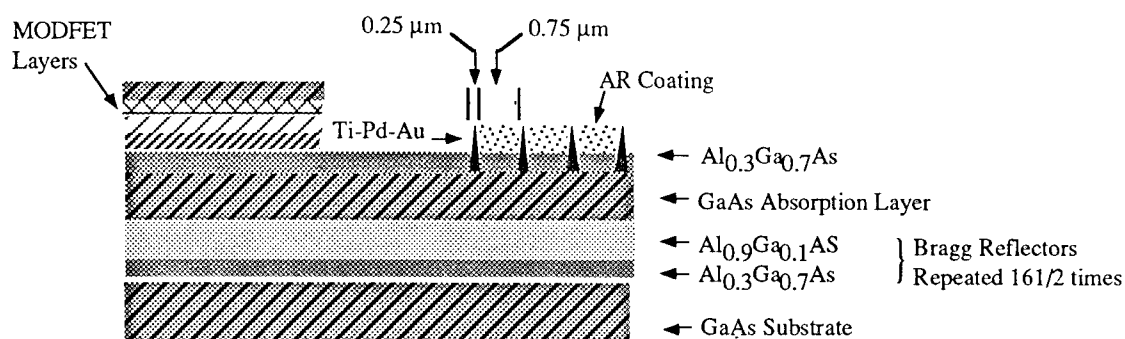
Fig. 1. Cross-sectional view of the metal-semiconductor-metal photodiode. The quarter wavelength Bragg reflector layers ensure the reflection of the light to maximize the absorption. The half wave length cap layer on the top of the absorption layer decreases surface recombination rate and helps to trap the light inside of the absorption layer. The finger width and the spacing between the fingers are varied.

In designing and calculating the reflectivity and absorption of the detector layer structure, a complex dielectric function was used. The fundamental optical constants such as refractive index n, extinction coefficient k, and real and imaginary part of dielectric constant $e=e_1+i\,e_2$ can be calculated from the energy band structure of a material via the optical joint density of states (JDOS)[3]. With the optical constants calculated, a transmission matrix

4

method[4] was used to calculate the total reflectance of the surface. The calculated optical response for a 770 nm light design is shown at Figure 2.

From these calculations, the layer structures were optimized to minimize the surface reflectance. According to the layer optimization, photodetector layers were grown. The calculated and measured surface reflectance of the photodetector layers agreed well, showing 0.5 % of the reflectance from the top surface at the designed wavelength of light.

III. MSM Photodetectors

The inter-digitated MSM photodetectors were fabricated on the MBE grown wafers by using optical and E-beam lithography in various dimensions. Figure 3 (a) shows a detector with 0.75 μm gap and 0.25 μm finger. The topology of a microwave equivalent circuit model for the detector diodes was determined using S-parameter measurements of the devices and of associated short circuited test structures. The S-parameter measurements on the short circuit test structure readily allow for the extraction of the finger electrode resistance and inductance. In addition to the DC resistance in the fingers, there is a frequency dependent skin effect resistance. The skin effect resistance is proportional to the square root of the frequency. The proportionality constant can be determined by comparing the frequency dependence of the measured device input impedance with that of the model. The MSM detector capacitance is extracted from the device measurements and the excess parasitic capacitance is determined by comparing the measured capacitance to that calculated for an MSM structure using the conformal mapping technique[2][5]. The parasitic capacitance is the result of the finite length of the interdigitated fingers and the proximity of the contact
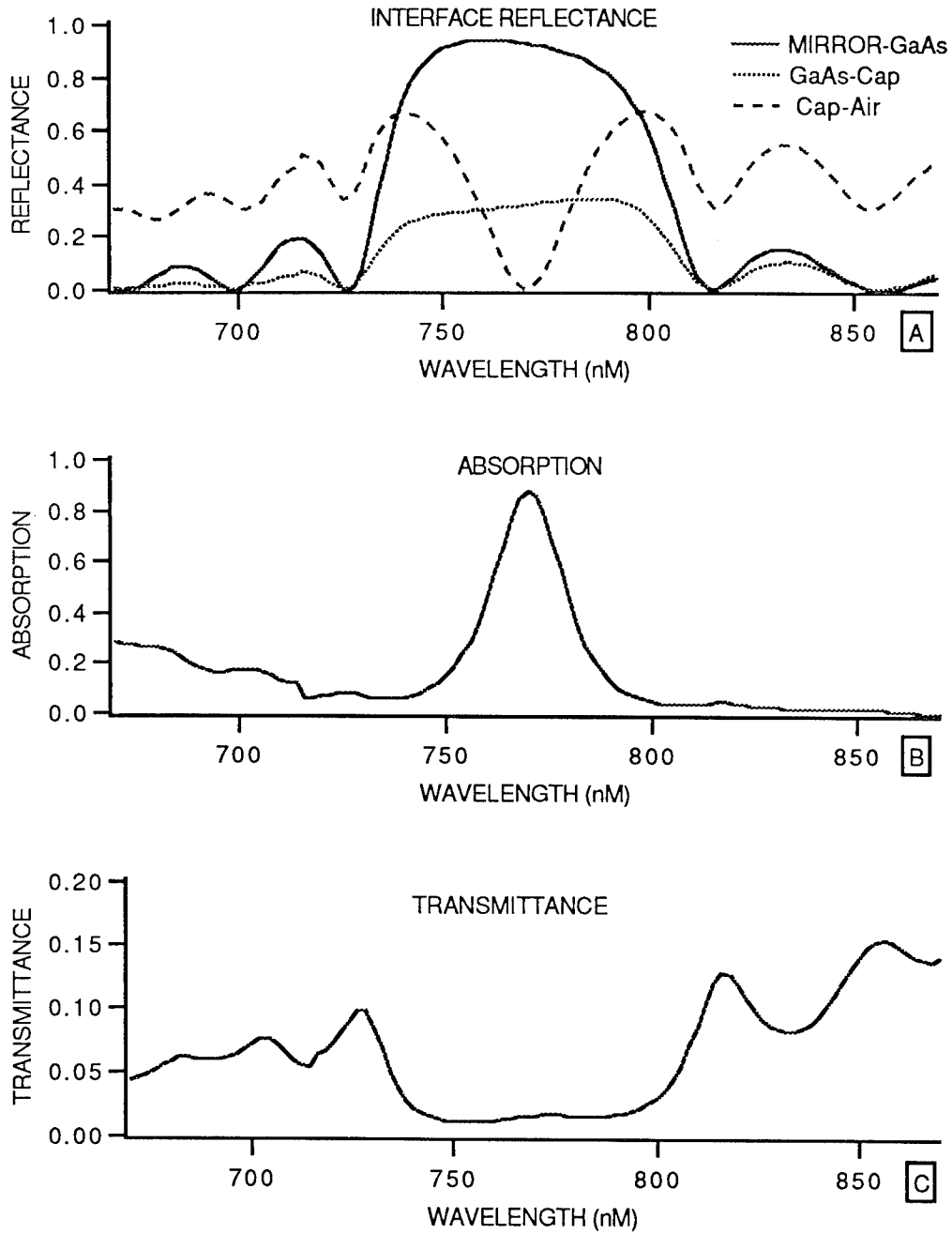
Fig. 2. The calculated optical response of the detector material layers for a 770 nm light design: (a) Reflectance at important interfaces of the structure. (b) Fraction of incoming light absorbed. (c) Fraction of incoming light transmitted into the substrate.
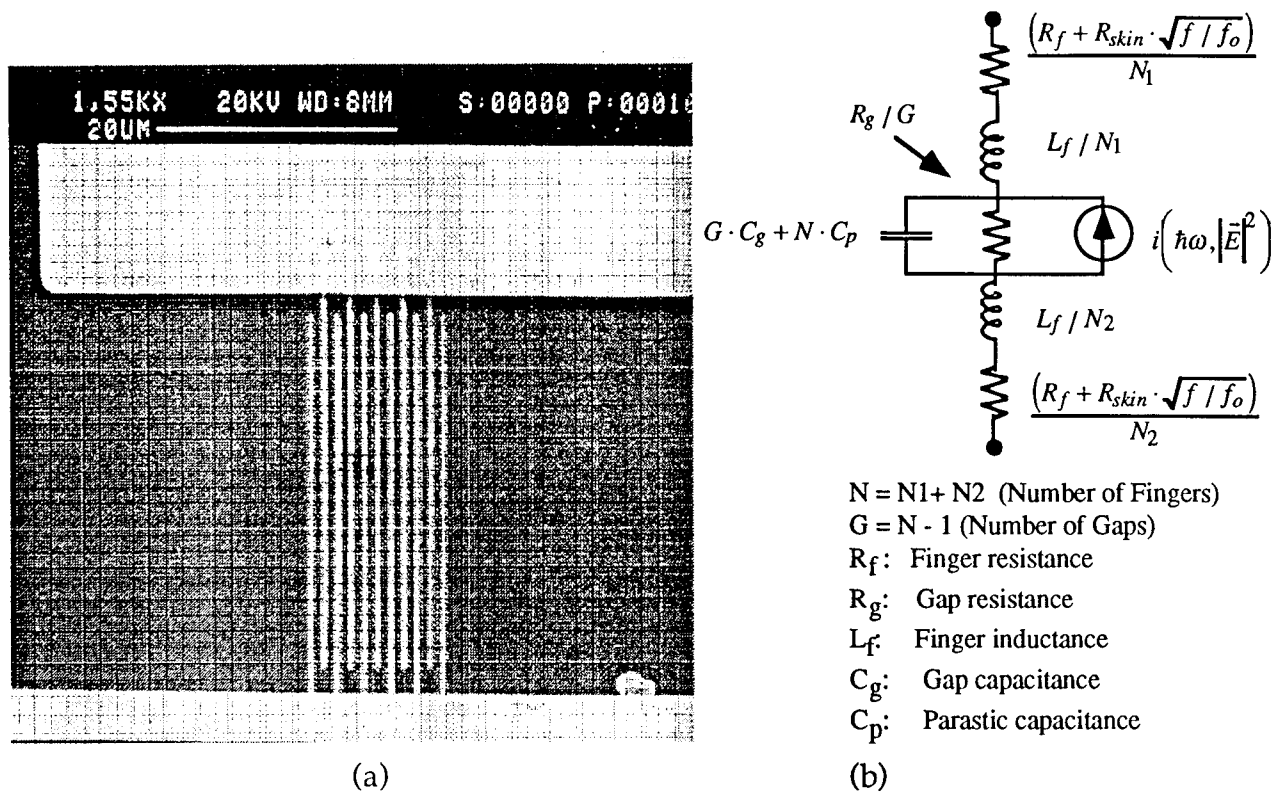
$$G \cdot C_g + N \cdot C_p$$

$$\frac{\left(R_f + R_{skin} \cdot \sqrt{f / f_o}\right)}{N_1}$$

$$L_f / N_1$$

$$R_g / G$$

$$L_f / N_2$$

$$\frac{\left(R_f + R_{skin} \cdot \sqrt{f / f_o}\right)}{N_2}$$

$$i\left(\hbar\omega, |\vec{E}|^2\right)$$

$N = N1 + N2$ (Number of Fingers)
$G = N - 1$ (Number of Gaps)
R_f : Finger resistance
R_g : Gap resistance
L_f : Finger inductance
C_g : Gap capacitance
C_p : Parastic capacitance

(a)   (b)

Fig. 3.   (a) An MSM photodetector with 0.25 μm finger and 0.75 μm gap. Ti
150Å, Pd 150Å, and Au 500Å were used for finger metalization. The
pad connecting the fingers is a part of a coplanar waveguide.   (b)
MSM detector diode equivalent circuit model.

pad of opposite polarity to the open ends of the fingers.   The equivalent
circuit model (Fig. 3 (b)) is used to determine the passive element frequency
response and time domain impulse function.

The transport characteristics of the optically generated carriers are studied
using a Monte Carlo simulation[6].   The carrier responses are simulated for a
given detector geometry, light wavelength, and applied bias to obtain the time
domain response.   In this calculation, polar optical scattering, acoustic
phonon scattering, and intervalley scattering are considered, the interaction
between the carriers neglected.   The fast Fourier transformed (FFT) result of
the time domain response provides frequency domain response.   This
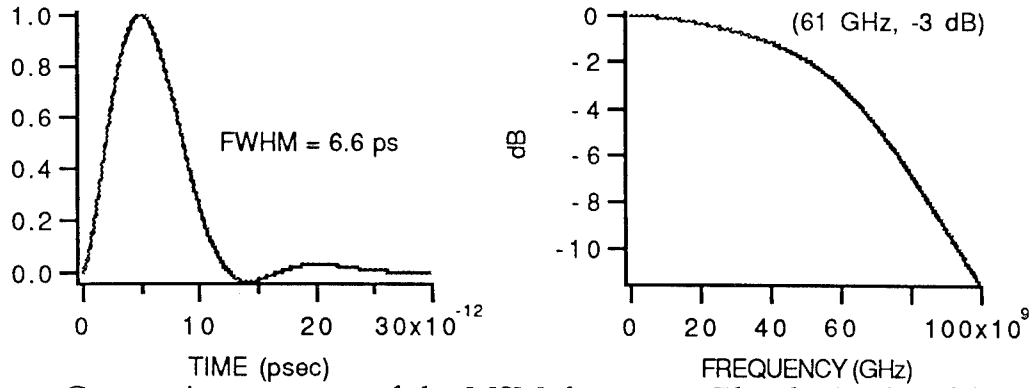intrinsic carrier response is combined with the circuit

Fig. 4. Composite response of the MSM detector. The device has fifteen 23 μm long fingers with 0.5 μm finger width and 0.5 μm gap.

response to produce the composite frequency response and impulse function of the MSM detectors (Fig. 4). The resultant 3dB bandwidth is 61 GHz for a 0.5 μm gap detector.

A frequency response measurement was done using a HP2782 spectrum analyzer and a mode-locked short pulsed (120 fs) laser. A 23 μm long detector with 0.5 μm finger width and 0.5 μm gap between fingers was tested using 780 nm light. At 7 V applied bias and 80 μW average power, it showed flat response at least up to 40 GHz, which was the limit of this measurement. When the average power of the incident beam increased to 160 μW, the response at 39 GHz was -6 dB down from the low frequency value due to excess carrier generation and resultant band flattening. Measured dynamic range using Ti-Sapphire laser at 770nm was in excess of 33 dB.

Quantum efficiency was measured for large scale (200μmx200μm) detectors with various etch depth of the AlGaAs detector cap layer. These devices had 1μm finger width and 2μm gap. The detectors showed gain when all the cap layer had etched (110% etch). This low frequency gain can be minimized by preserving some of the cap layer as shown at table 1. For 0% etched detectors, the quantum efficiency is a little low, as the optically generated carriers must pass through the thick cap layer. For 33% etched and 67% etched devices, quantum efficiency were 55-56% at 5V bias and 63-70% at 10V bias. By considering 33% of the detectors is covered with metal fingers, the internal quantum efficiency is 82-84% at 5V and 94-105% at 10V.

8

Bias	Quantum efficiency (external)			
	0% etch	33% etch	67% etch	110% etch
1V	28%	52%	49%	40%
5V	31%	55%	56%	238%
10V	44%	63%	70%	950%

Table 1. Quantum efficiency with various etch depth of the cap layer. 200μmx200μm detectors had 2μm gap and 1μm finger.

Due to the Bragg reflector layers beneath the absorption layer, the detectors show wavelength dependent responses. We measured the current from the detector varying the wavelength of the incident light. A white light source and a monochromator were used for this measurement. For a 23 μm long detector with 1 μm finger width and gap on the wafer for 800 nm light design, the electrical current from the detector normalized to the incident light power showed a major peak around 790 nm (Fig. 5). This shift is attributable to the fact that the incident light was not quite normal.
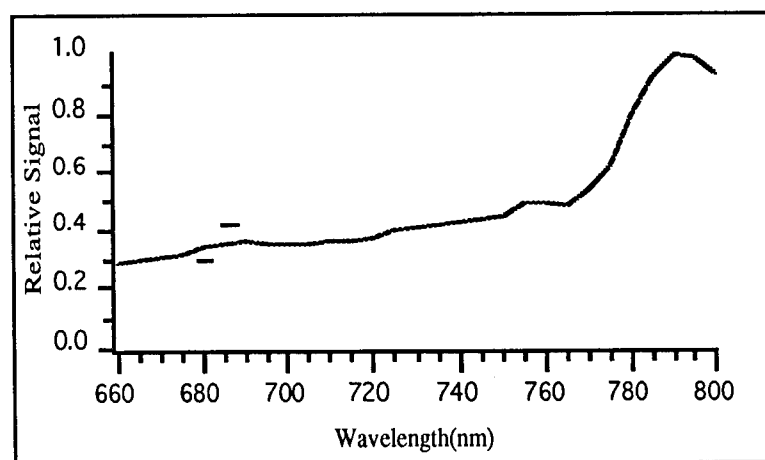
IV. Circular Photodetectors

Fig. 5. Relative signal from a detector vs. optical wavelength. The detector was fabricated on the wafer designed for the absorption of 800 nm light.

The capacitance of MSM photodetectors is calculated using a conformal mapping technique [5], and roughly proportional to the total area of the

photodetectors [2]. The advantage of using a circular-shaped detector (Fig. 6) as opposed to a square-shaped detector is that a circular-shaped detector minimizes the device capacitance and also matches the shape of the incident light beam which is usually emanating from an optical fiber or a laser. A rectangular or square detector will waste area because the beam can never fit exactly inside the device periphery. For the detection of a beam with diameter d, the minimum area required is $\pi d^2/4$ for a circular detector and d^2 for a square detector. The smaller area of the circular detector also leads to a reduced capacitance by a factor of 79%. Circular detectors with concentric semi-circular fingers (Fig. 6 (a)) were fabricated on an MBE grown GaAs based detector layer. The measured capacitance and parasitic inductance obtained from S-parameter measurements for the detectors, 20μm in diameter, are 19.9fF and 183pH respectively. The long thin center stem of this geometry generates high inductance. The second type of circular detector has been developed which avoids the problems of the long center stem (Fig. 6 (b)). This second geometry utilizes linear fingers of different lengths to form a curved periphery. For this circular detector with linear fingers and 65μm in diameter, fabricated on the same detector layer, the measured capacitance is

(a)   (b)
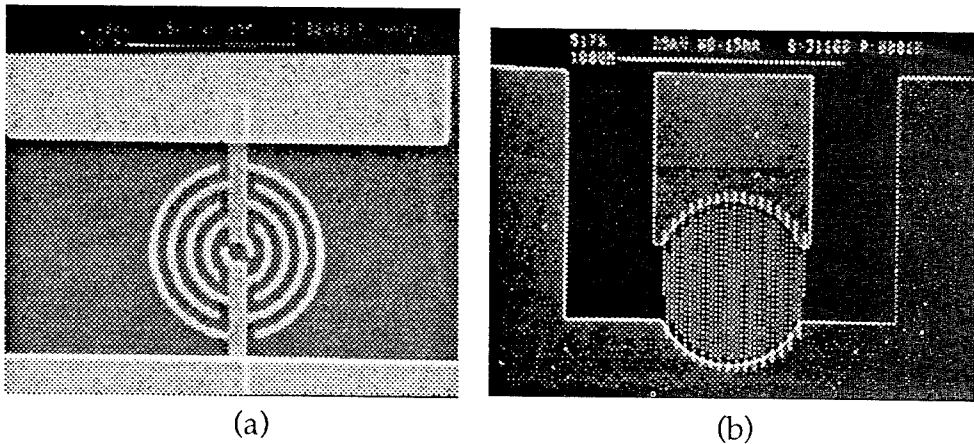
Fig. 6 (a) A circular photodetector with concentric semi-circular fingers, 20 μm in diameter. (b) A circular detector with linear fingers, 65μm in diameter.

140 fF and the inductance is 46pH. The larger capacitance of the circular detector with linear finger, compared with the other type of circular detectors was from the bigger size of the detector.

V. Optimization of MSM Photodetectors

Calculating the 3dB bandwidth of a photodetector, transit time response of the optically created carrier response in the photodetector and RC circuit response are the two things to consider. The 3dB bandwidth f_{RC} of an RC circuit is given by

$$f_{RC} = \frac{1}{2\pi RC}.$$

(1)

For transit time response, there are several factors in addition to the detector geometry which determine the ultimate frequency response of the device including absorption layer material and thickness, applied bias, light wavelength and the intensity of the incident beam. Thus one must be careful in comparing the results of different researchers. For example two groups measuring devices with 0.5μm gap between the fingers reported quite different 3dB bandwidths, 105GHz and 50GHz [7], [8]. Given the uncertainty due to the above listed factors, we can use a simple first order estimation of the transit time. The first order approximation of carrier transit time t_{tr} and its 3dB bandwidth f_{tr} are given by

$$t_{tr} = \frac{1}{2}\frac{g}{v_s}\eta, \quad \text{and} \quad f_{tr} = \frac{1}{2\pi t_{tr}}$$

(2)

where v_s is the carrier saturation velocity, g is the gap width between the fingers, and η is a corrective constant of order unity. In this approximation the transit time of the carriers is taken to be the time required to travel half of the gap width. This approximation is valid when the electric field is high enough to saturate the carrier velocity, which is usually the case, and when absorption layer thickness is small compare to gap. A thin absorption layer may result in low quantum efficiency. However, a thin absorption layer, 250nm, has been employed to obtain higher bandwidth [8] and the layer structure that we are working on is expected to have more than 90% internal quantum efficiency with 312nm absorption layer using Bragg reflector layers and a cap layer. Therefore the thin absorption layer approximation is not so far from the reality, though care must be taken for the very small gap detectors. We can get some ideas of what η would be by comparing f_{tr} from eq. (2) with the above two reported results of 50GHz [8] and 105GHz [7] for a 0.5μm gap detector. Taking the carrier saturation velocity to be 1×10^7 cm/s, η is 0.61 at 50GHz and 1.3 at 105GHz.

The RC circuit response, eq. (1), and the intrinsic carrier response, eq. (2), must be considered together in order to determine the overall 3dB bandwidth of the detectors. These two responses can be combined to give a simple first order approximation to the overall 3dB bandwidth of the MSM detectors as follows.

$$f_{3dB} \approx \frac{1}{2\pi\sqrt{t_{tr}^2 + (RC)^2}} \qquad (3)$$
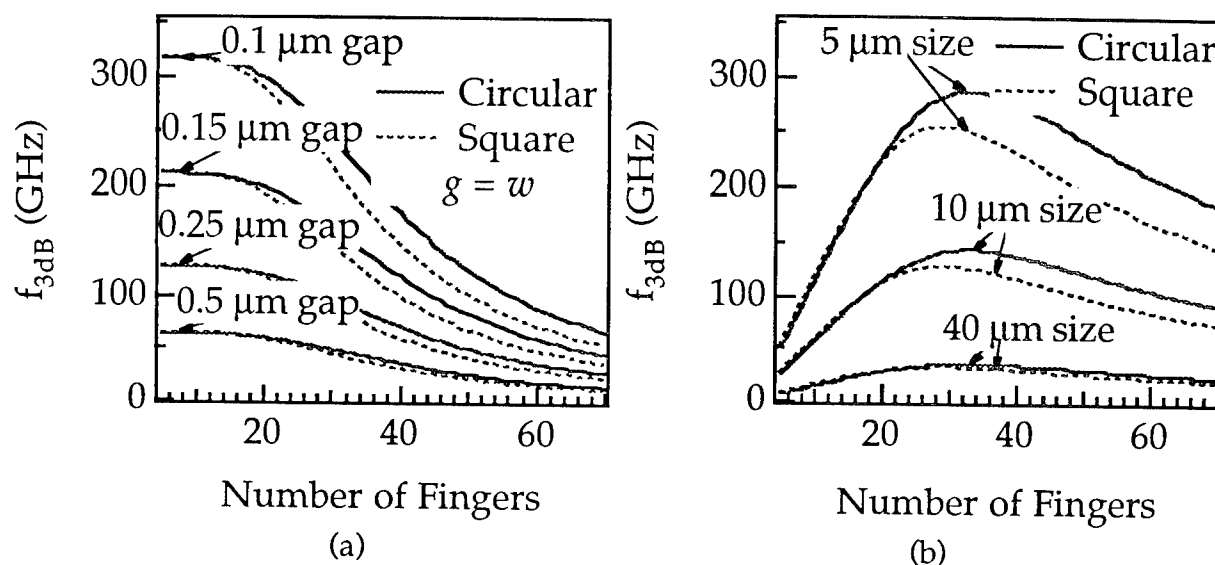
Fig 7. (a) The calculated f_{3dB} as a function of the number of fingers for the constant gap detectors. The constant gap detectors have the same finger width w and gap g. η is 1 for this calculation. (b) The calculated f_{3dB} as a function of the number of fingers for constant size detectors. The calculation is done with h equal to 1 and the load resistor R equal to 50 W. The finger width is the same as the gap. The optimum number of fingers where f_{3dB} is maximum remains the same as the detector size varies. Circular detectors (solid lines) show maximum f_{3dB} at 33 number of fingers and square detectors (dashed lines) at 29.

The calculated overall 3dB bandwidth is plotted in figures 7, using a load resistor of 50Ω. We neglected the parasitic inductance
and the additional resistance of the photodetector which is usually small. For this calculation the corrective constant η is set to be 1. Figure 7 shows the calculated 3dB bandwidth for detectors with constant gaps. For these

12

photodetectors, the finger width w is the same as the gap width g. For the constant gap detectors, both the total detector size and the capacitance increase as the number of fingers increases. Thus the 3dB bandwidth decreases as the number of fingers increases for the constant gap detectors, due to the increase in the capacitance (Fig. 7 (a)). The 0.1μm gap curve in Fig. 7 (a), shows high bandwidth for small number of fingers, but there is not much detection area at this region.

Alternatively the detector area can be maintained constant while changing the number of fingers and adjusting the finger width and gap accordingly. In this case the 3dB bandwidth as a function of the number of fingers behaves differently from the constant gap scenario. As the number of fingers increases, the gap between the fingers must decrease, therefore the carrier transit time decreases but the capacitance increases. As a result the 3dB bandwidth increases at first, since the decreasing carrier transit time initially dominates the response. After a certain point the increasing capacitance will begin to dominate the frequency response and the 3dB bandwidth will fall off as more fingers are added (Fig. 7 (b)).An important point to note here is that the maximum 3dB bandwidth is always achieved with the same number of fingers regardless of the detector size. The optimum number fingers yielding the maximum 3dB bandwidth is 33 for the circular detectors, and 29 for the square detectors when the corrective constant η is 1. The total area A is approximately proportional to $(n \cdot p)^2$ for square or circular detectors, where n is the number of fingers and p is the period, which is the sum of g and w. For a given gap-to-period ratio, capacitance is roughly proportional to A/p, i.e. $\sqrt{A} \cdot n$ [2], and transit time is proportional to g or p, i.e. $\sqrt{A} / n$. Thus, taking the derivative of eq. (3) with respect to n and equating to zero yields the optimum number of fingers independent of the total area. The broad maximum allows a choice of from 27 to 41 fingers for circular detectors and from 24 to 36 fingers for square detectors to maintain more than 95% of the attainable maximum values, which permits more flexibility in design. As η varies, the optimum number of fingers changes accordingly, but for a given h the maximum bandwidth is always obtained with the same number of fingers regardless of the detector size. Table 2 summarizes the change of the optimum number of fingers and

13

the range of number of fingers having more than 95% of the maximum values for values of η obtained above.

η	Circular detectors		Square detectors	
	Optimum No.	95% Range	Optimum No.	95% Range
0.61	26	21-32	23	19-28
1.0	33	27-41	29	24-36
1.3	37	30-46	33	27-41

Table 2. The optimum number of fingers and range of number of fingers having more than 95% of the maximum values for a given corrective constant η.

VI. Fabrication of MODFET's

MODFET's (MOdulation Doped Field Effect Transistors) as post-detection amplifiers, play a vital role in optical receiver circuits. To amplify the 44GHz optical signal successfully, transistors are required to have high unity current gain frequency, f_t, and unity power gain frequency, f_{max}. A part of effort to improve the characteristics of the transistors, has been done developing 0.25μm gate-length gamma-shaped gate and self-aligned ohmic metalization to reduce the source resistance and the noise figure ultimately[9],[10]. (Fig. 8 (a)) The gate had an overhang ratio of 2:1 and a source-drain spacing of 0.6 μm. With this self-aligned metalization the source-gate spacing was 0.1 μm and the drain-gate spacing was 0.25 μm. In addition to the gamma gate process, we have also worked on short gate (<0.15μm) MODFET's on the same epitaxial layer containing pseudomorphic $In_{0.2}Ga_{0.8}As$ channel. (Fig. 8 (b))

The fabrication of the short gate MODFET's was done using standard MODFET process. After the putting alignment marks, mesa isolation etch was performed using wet chemicals. In this etching step, the surface reflectance were carefully monitored to obtain maximum absorption in the photodetector layer. Ohmic metalization followed the isolation step. The gate process was done at the end of all the optical receiver processes to avoid any damages to the short gates. In the gate process, tri-level electron beam resists composed of PMMA and PMMA co-polymer were used. After the gate exposure using the electron beam, about 70nm in diameter, gate recess etch was done to remove highly doped GaAs cap layer. For gate metals Ti/Pd/Au were used.

14

The fabricated transistors had gates 150μm in width and 0.12μm to 0.14μm in length. The transistors showed 110GHz of f_t, and 60GHz of f_{max}. Transconductance was around 450mS/mm. For these transistors, f_t was higher than f_{max}, due to the high gate resistance and high Gds, source-drain shunt conductance.

(a)

(b)

(c)

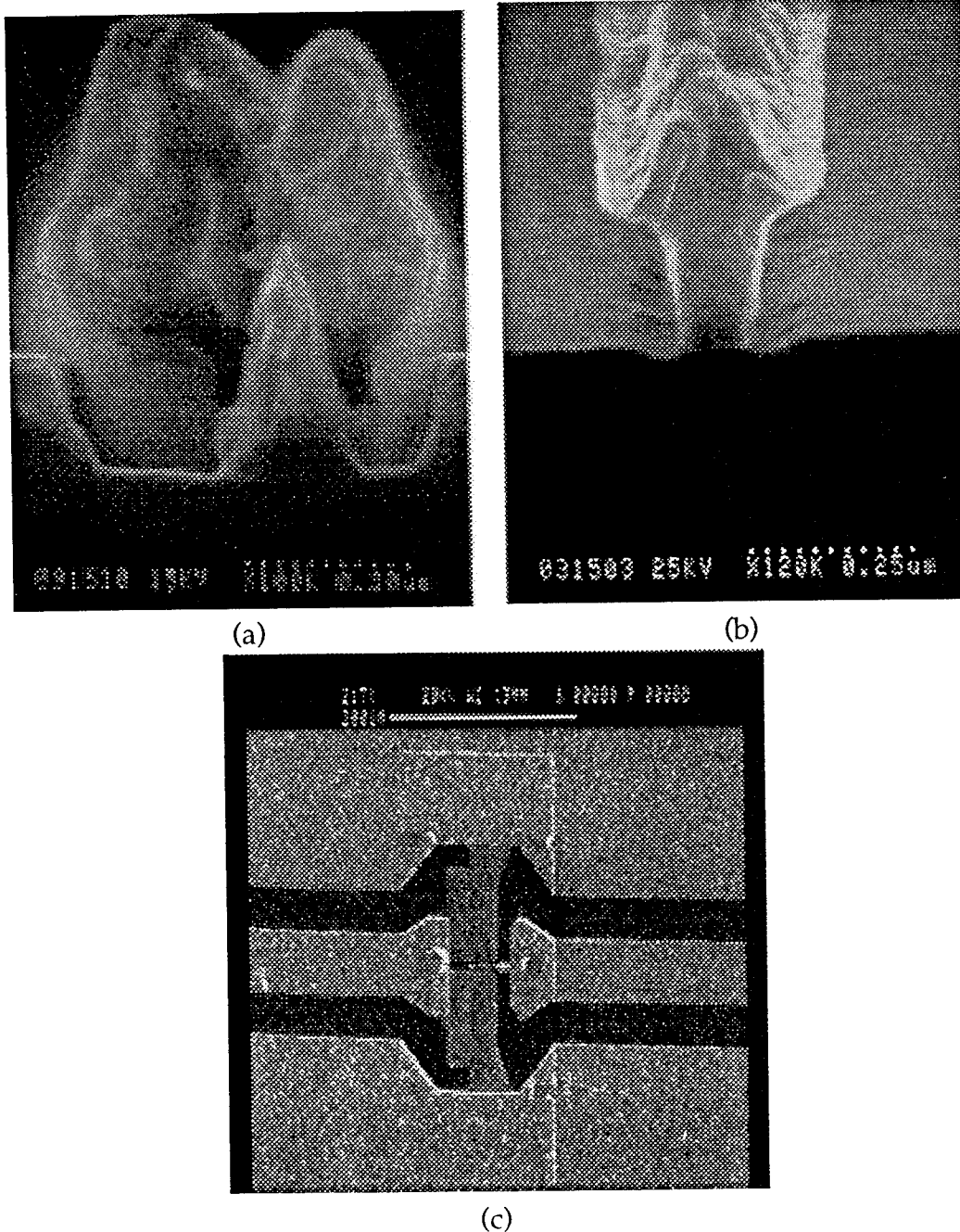Fig. 8 (a) Gamma-gate with 0.25 μm footprint and 2:1 overhang ratio. The photograph also shows the 0.6 μm drain - source spacing after the self-aligned ohmic metalization step. (b) 0.12 μm long T-shaped gate cross-

15

section. (c) 150 μm gate width MODFET in coplanar waveguide structure.

VII. Integrated Optical Receiver Circuit Design

For high frequency amplifying circuits, proper impedance matching is essential to maximize the transmission of signal. However, the impedance matching is not trivial to accommodate DC bias lines and capacitors at high frequency. For the optical receiver circuit design, we fabricated each element individually and measured the S-parameters at 44GHz, where the circuit is designed to operate. Each element was comparable to coplanar waveguide (CPW) structure and could be probed using Cascade probes. From these measured S-parameters, the circuits were designed to maximize the flow of signal. The circuits contain a photodetector, either one or two transistors, DC bias lines, blocking capacitors and CPW impedance matching networks. (Fig. 9) DC bias lines and capacitors were carefully arranged not to interrupt the flow of signal. The main purpose of the capacitors was DC blocking. In designing the circuits, we devised three different DC bias schemes,
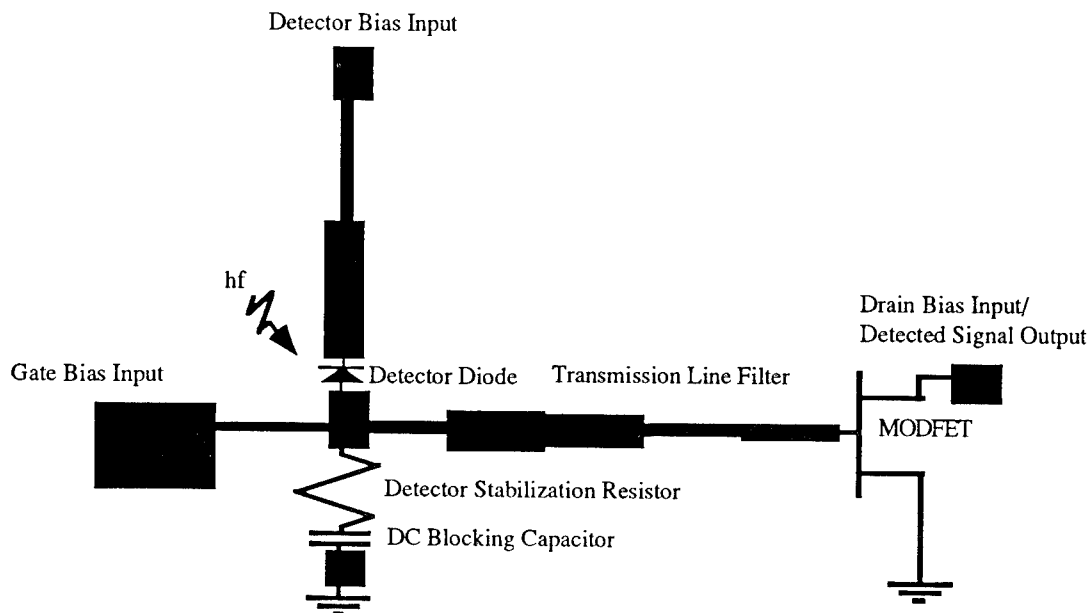
Fig. 9. Schematic diagram of an integrated optical receiver. In the actual circuit coplanar waveguides will be used for the transmission line interconnections

16

(1) wavetraps and resistors, (2) DC blocking capacitors at the ground plane of the CPW, and (3) CPW lines with DC blocking capacitors at the center plane of CPW.

In case of a single stage amplifier containing a detector and a transistor, three DC bias lines are required, each one for the detector and for the gate and the drain of the transistor. The drain bias is usually achieved by Cascade probes to a network analyzer where bias T is internally built-in. Thus only two bias lines are needed to be considered. A wavetrap is an alternating sequence of high and low impedance lines of quarter wavelength each. A wavetrap having low impedance lines at both ends, its input impedance will be minute at high frequency. As the end of the wavetrap is a virtual ground having very small input impedance, the end of the wavetrap can replace a part of ground plane. At the same time, this wavetrap allow us to apply a bias as it is not connected to the ground plane. For biasing, an adequately large resistor (~500Ω) will be used to connect the end of a wavetrap to a transmission line, where a DC bias is needed, to block any significant RF signal pass through the resistor. To have two separate biases to a detector and the gate of a transistor, two wavetraps and a resistors were used. For the resistor, Ti-evaporated thin film resistor was used. An advantage of using wavetraps as bias lines is at its easiness in fabrication as we can avoid the use of capacitors. However device size tends to be bigger due to long wavetraps. (Fig. 10)
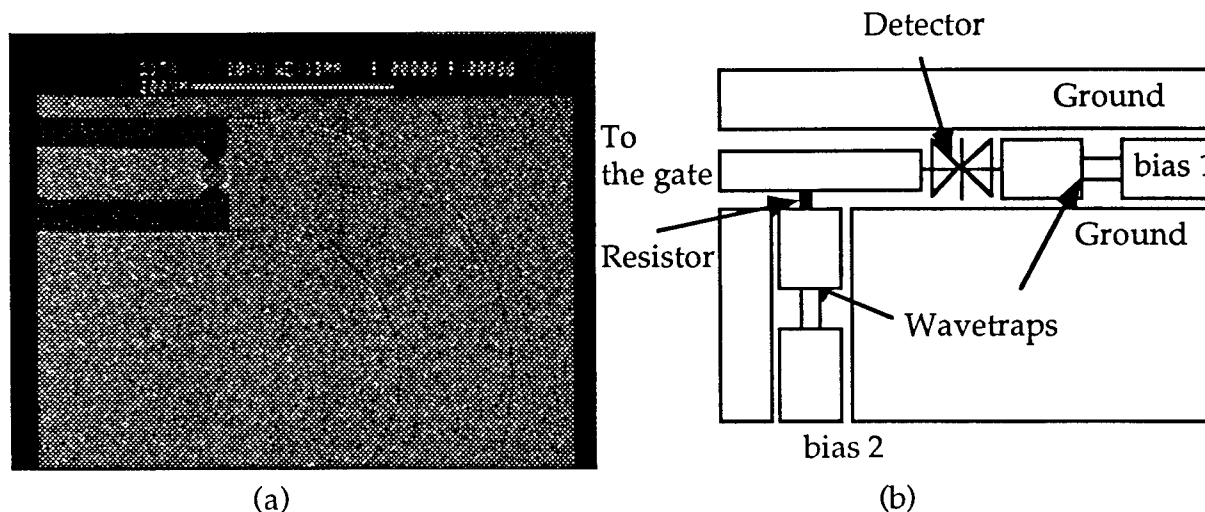

(a)   (b)

Fig. 10 (a) A photodetector with a wavetrap in CPW. (b) A bias scheme using two wavetraps and a resistor.

By using DC blocking capacitors at the ground plane of CPW, separate bias can be applied as well. In this case, we bias a section of the ground plane of CPW instead of biasing the center transmission lines corresponding to the ground plane. The fabrication of overlay capacitors involves bottom metal, dielectric, and top metal evaporations. E-beam evaporated SiO_2 was used for the dielectric film. The circuits of this bias scheme are compact in size, which allow us to utilize the area to the maximum. (Fig. 11)

(a)   (b)
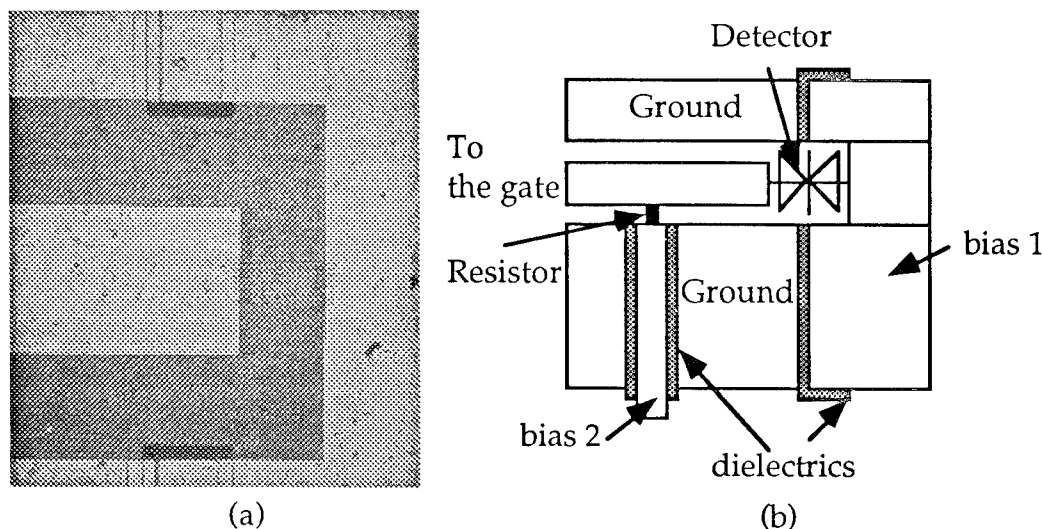
Fig. 11 (a) A photodetector with capacitor isolations. (b) Bias scheme using capacitor isolations.

The third bias method is to use CPW bias lines. The CPW bias line must be designed so that little RF signal penetrates into the line. For this purpose, we used quarter wavelength high impedance lines with capacitors at one end. For a high frequency signal, a capacitor in a circuit can be treated as a short, and one end of a quarter wavelength line with a short at the other end will be an open. Thus our quarter wavelength CPW bias lines with capacitors at one end is an open at the other end and it is not easy for a RF signal to pass through. To ensure the RF blocking, double sections of a quarter wavelength bias line and a capacitor were employed. The bias lines were fabricated and tested showing minimal signal penetration. (~-50dB which was about the limit of the measurement.) (Fig. 12)

Each bias scheme was tested after the fabrication. The wavetrap bias lines and capacitor bias scheme didn't influence the transmission of signal much, showing -0.28dB and -0.13dB insertion loss at 44GHz, respectively. However,

CPW bias lines showed -0.95dB insertion loss at 44GHz. This was due to the openings at the ground plane to connect the CPW bias lines. This undesired effect can be reduced by using bonded wires to connect the separated ground planes as shown at figure 12.
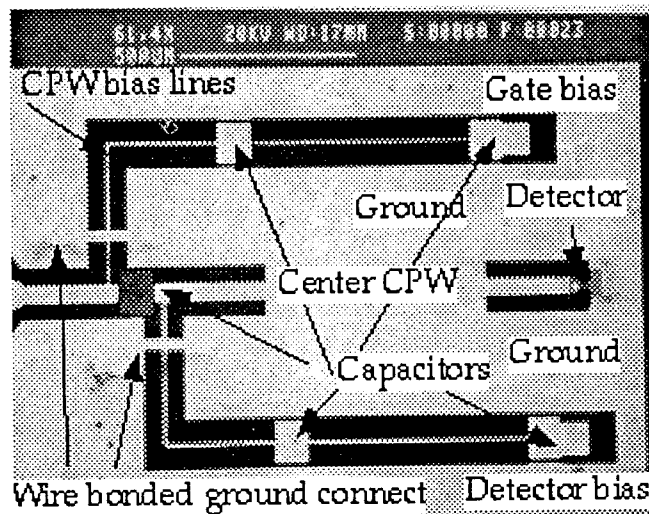
Fig. 12 A circuit with CPW bias lines.

According to the schemes developed, optical receiver circuits have been fabricated and are ready for testing. For photodetectors, both circular and rectangular ones were employed. The receivers are tuned for narrowband detection of a 44 GHz modulation signal being transmitted on the 770 nm optical carrier. The circuits employ input and output impedance matching networks. The circuit shown at figure 13 contains a single stage amplifier with the input taken from a linear MSM detector. The detector and transistor were DC isolated by an SiO_2 overlay capacitor and CPW bias lines were used. We used a CAD program, Touchstone, to estimate the resultant

Figure 13. Single Stage Monolithic Optical Receiver Circuit.

19

gain from a circuit. From the measured value of the transistors and the simulated values for the other components, a single stage amplifier showed 6.6dB gain over the detector output. (Fig. 14) The overall optical receiver gain, including the photodetector signal drop, was 5.7dB at 44GHz

VIII. Conclusions

The circular shaped MSM photodetectors have been introduced as an endeavor to decrease the capacitance of the devices. The circular geometry may reduce the capacit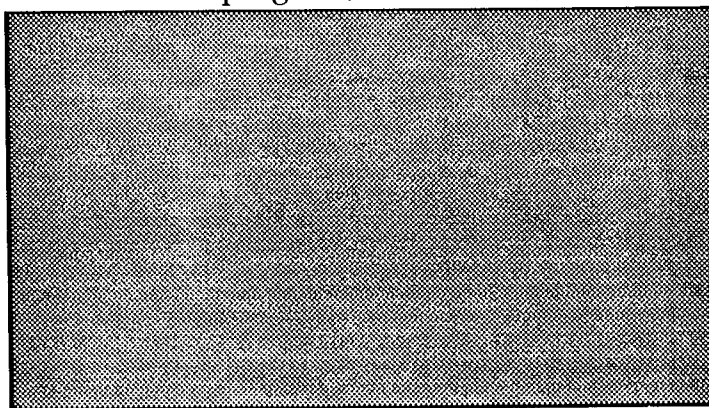ance of a comparable square detector by up to 21%. The first order calculation that we suggested is not exact, however it is quite useful in providing insight for design purposes.   From the above calculated capacitance and
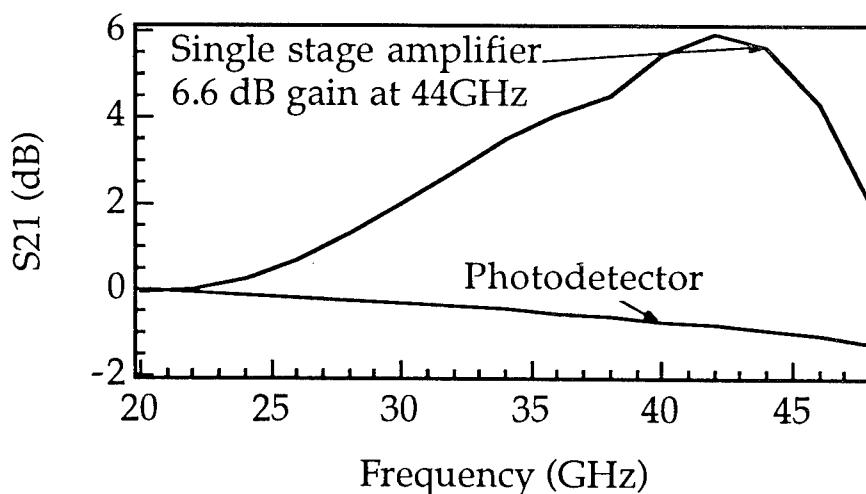
Fig. 14 A simulated gain of single stage amplifier. Measure transistor values were used with the other calculated values.

transit time, the 3dB bandwidths and the optimum numbers of fingers for the photodetectors were obtained.   The optimum number of fingers is 29 for square aperture detectors and is 33 for circular aperture detectors.
We fabricated both conventional rectangular-shaped and circular shaped detectors on MBE grown wafers.   The detector layer structures, employing buried Bragg reflector layers below the absorption layer for the additional absorption, were designed and optimized to minimize the surface reflectance.

20

Device measurements of 0.5 µm finger width and 0.5 µm gap detector show the 3 dB bandwidth in excess of 40 GHz with dynamic range more than 33 dB. The problems of long time response tail and low frequency gain, due to the surface exposure of the GaAs absorption layer, has been solved by etching the cap layer less and deposited metal fingers on AlGaAs cap layer. The fabricated MSM interdigitated photodetector with 2µm gap on the detector layer, through etching only 33% of the cap layer, showed the internal quantum efficiency of 82% at 5V bias and of close to 94% at 10V bias.

As post-detection amplifiers, we fabricated pseudomorphic $In_{0.2}Ga_{0.8}As$ channel MODFET's. Employing 0.12µm to 0.14µm long gate, we could achieve 110GHz of f_t and 60GHz of f_{max}. f_{max} can be improve more by optimizing the layout of the transistors.

In designing a optical receiver circuit, three different schemes in DC biasing were developed. Among these three, the use of DC blocking capacitor at the ground plane yielded the lowest insertion loss of -0.13dB at 44GHz. The bias line using wavetraps and resistors showed its advantage of easy fabrication and low insertion loss (-0.28dB at 44GHz).

The optical receiver circuits have been fabricated with either a rectangular or a circular photodetector and with one of the above bias schemes. The circuits are ready for optical tests. A computer simulation showed 6.6dB gain of single stage amplifier at 44GHz. The overall optical receiver gain, including the photodetector signal drop, was 5.7dB at 44GHz.

IX. Acknowledgment

X. References

[1] Y. Chen, S. Williamson, T. Brock, F. W. Smith, and A. R. Calawa, "375-GHz-bandwidth photoconductive detector," Appl. Phys. Lett., vol **59**, pp. 1984-1986, 1991.

[2]   S. Y. Chou and M. Y. Liu, "Nanoscale Tera-Hertz Metal-Semiconductor-Metal Photodetectors," IEEE J. Quantum Electron., vol **28**, pp. 2358-2368, 1992.

[3]   S. Adachi, "Optical properties of $Al_xGa_{1-x}As$," Phys. Rev. B 38, pp. 12345-12352, 1988

[4]   W. W. Lui, M. Fukuma, "Exact solution of the Schrodinger equation across an arbitrary one-dimensional piecewise-linear potential barrier," J. Appl. Phys., vol 60, pp. 1555-1559,1986

[5]   Y. C. Lim and R. A. Moore, "Properties of Alternately Charged Coplanar Parallel Strips by Conformal Mappings," IEEE Tran. Electron Devices, vol **ED-15**, pp. 173-180, 1968.

[6]   L. Reggiani, "General Theory," Hot-Electron Transport in Semiconductor, L. Reggiani ed., Chapt. 2, Springer-Verlag, Berlin Heidelberg, 1985

[7]   B. J. Van Zeghbroeck, W. Patrick, J.-M. Halbout, and P. Vettinger, "105-GHz Bandwidth Metal-Semiconductor-Metal Photodiode," IEEE Electron Device Lett., vol **9**, pp. 527-529, 1988.

[8]   C. Moglestue, J. Rosenzweig, J. Kuhl, M. Klingenstein, M. Lambsdorff, A. Axmann, J. Schneider, and A. Hülsmann, "Picosecond pulse response characteristics of GaAs metal-semiconductor-metal photodetectors," J. Appl. Phys., vol **70**, pp. 2435-2448, 1991.

[9]   L. D. Nguyen, P. J. Tasker, D. C. Raduescu, and L. F. Eastman, "Design, Fabrication, and Characterization of Ultra High Speed AlGaAs/InGaAs MODFET's," IEDM Tech. Digest, pp. 176-179, 1988

[10] R. C. Tiberio, J. M. Limber, G. J. Galvin, and E. D. Wolf, "Electron Beam Lithography and Resist Processing for the Fabrication of T-Gate Structure," SPIE Vol. 1089, Electron-Beam, X-ray and Ion Beam Technology: Submicrometer Lithographies VIII, pp. 124-131, 1989.

II. Waveguide Metal-Semiconductor-Metal Photodetectors
for a 44 GHz Integrated Preamplifier
M.H. Leary and J.M. Ballantyne

Introduction

This report describes the work done to develop MSM waveguide photodetectors for an integrated 44GHz photoreceiver. The report is divided into two major sections. The first section summarizes the results reported in the 1992 and 1993 Annual Reports. The second section describes new work done in the final year of the contract.

Summary of Previous Work

The work described in previous reports covers the design of the photodetectors and process development for their fabrication. The paper "Waveguide Photodetectors for Monolithic OEIC's," by M. Leary and J. Ballantyne, included in Appendix A, is an excellent summary of this work. The following is a very brief overview.

I. DESIGN

The detectors were designed not only to operate at 44GHz, but also to be compatible with a standard high electron mobility transistor. To this end, we designed a special layer structure that meets both the optical waveguiding requirements of the detectors and the need for a high mobility modulated electron channel in the HEMT. A pseudomorphic InGaAs quantum well serves as both the electron channel and the optical absorber. We were able to vary the thicknesses of some of the layers to achieve the optimum balance between parasitic absorption at the electrode surfaces and detectable absorption in the quantum well. The electrodes were spaced to give a 3dB bandwidth of 50GHz.

Several sources of parasitic losses were accounted for. Scattering of light out of the waveguide is negligible and was ignored. Radiation of the guided mode into the substrate was calculated and the structure was designed to made this loss negligible. Absorption in undesirable regions was reduced with quantum well disordering to make the material transparent in definable

23

regions. Resistive loss at the electrode surfaces is the largest source of loss, and was the only loss explicitly used in the detection efficiency optimization. Assuming 100% conversion of photons to electron-hole pairs and an electrical internal gain of 1, the detection efficiency of these structures should be about 90% with detectors that are 1/8 of the modulation length at 44 GHz.

II. PROCESS DEVELOPMENT

We developed a process for the fabrication of these photodetectors that features self-aligned quantum well disordering and self-aligned electrode metallization. First, a layer of silicon nitride (SiN_x) is deposited and patterned. This layer acts as a barrier to the quantum well diffusion process. Next a thick silicon dioxide (SiO_2) layer is deposited to act as a catalyst for disordering, a ridge etch mask, and a metal definition mask. The SiN_x and SiO_2 layers both need to withstand the high temperatures (850-950°C) of the disordering process, so special low-pressure, high temperature techniques were developed to deposit these films by plasma-enhanced chemical vapor deposition. After the thick SiO_2 has been patterned, the ridges are etched with a selective etch which stops at a thin AlGaAs layer. This etch was developed this year and is described in detail later in this report. Next, the disordering is performed and finally the metal is defined, deposited, and lifted off. The technique for defining the metal at the base of the waveguide ridges was refined this year and is described later. A more detailed description of the fabrication process is given in Appendix A.
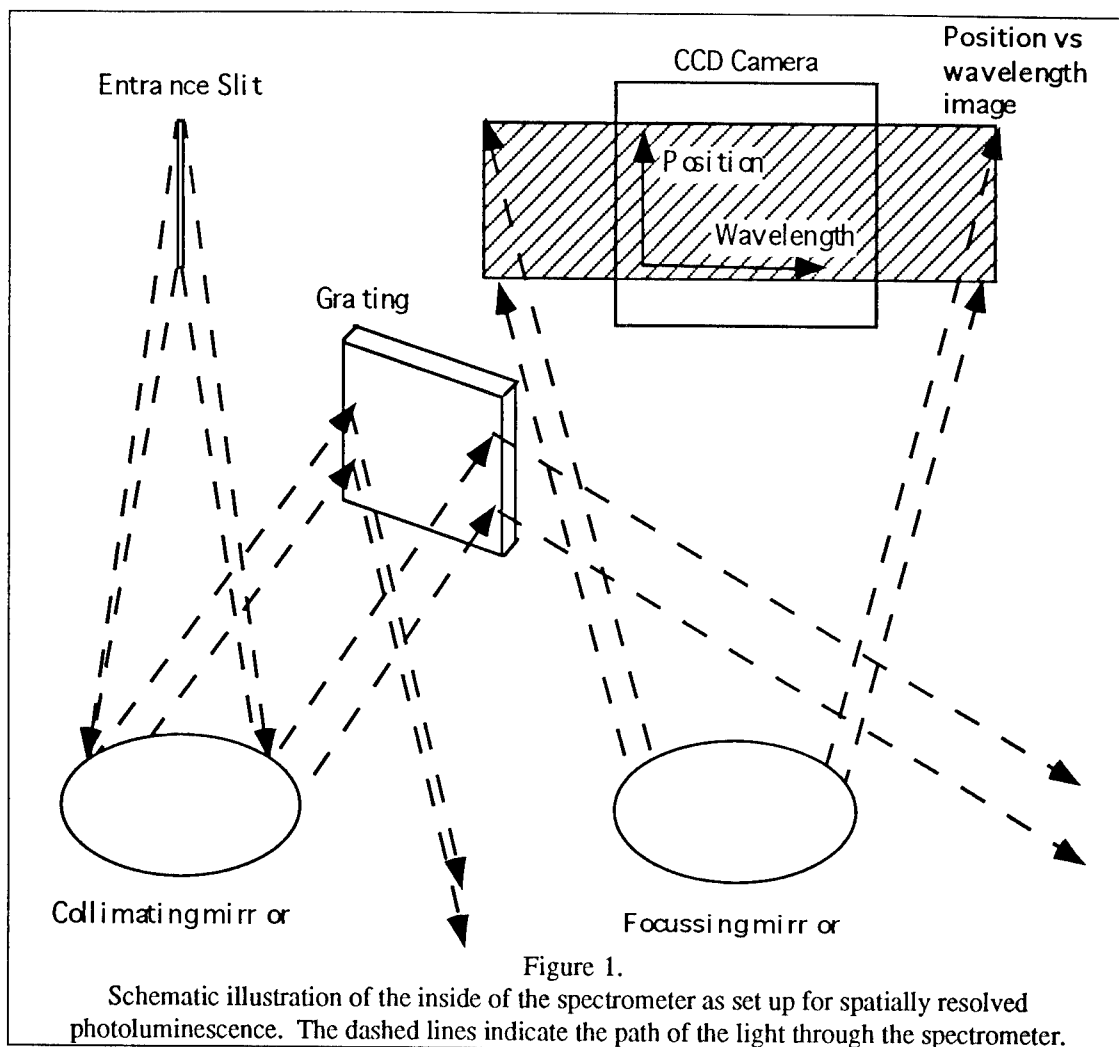
New Work 1993-1994

I. OVERVIEW

The majority of the work done in the last year of the contract focussed on finalizing the process sequence for the fabrication of the detectors. Integral to this goal was characterization of the quantum well disordering step to determine the optimal anneal temperature and time to achieve sufficient suppression of the optical absorption in the disordered regions relative to the non-disordered regions. We also need to know how the lateral extent of the disordering is affected by these parameters to ensure that the disordering does not spread too far sideways and ruin the device. In order to achieve these goals, we developed a system to take spatially resolved photoluminescence measurements. In addition to developing this system, we completed the development of the processing sequence for the detectors.

II. SPATIALLY-RESOLVED PHOTOLUMINESCENCE SYSTEM

The quantum well disordering step in our process is used to render the QW region transparent in regions outside the photodetector active region. Performing optical absorption measurements at various stages in the disordering process would provide a very direct characterization of the disordering process, but would require special test structures to be fabricated. Photoluminescence measurements, however, can provide information related to the optical absorption without requiring special test structures. Specifically, low pump intensity PL measurements reveal the bandgap energy and give an idea of the shape of the absorption curve on the low-energy side of the absorption edge.

Because we intend to fabricate undisordered regions only 0.9 μm wide in the middle of a field of disordered material, we also need to know the distance scale for the transition between disordered and non-disordered material. Because of the small dimensions involved, simply scanning a laser spot across the sample will not provide the required resolution. Instead, we developed a system using a square CCD array in a spectrometer which allows us to take PL spectra at narrowly spaced points along a line on the sample. The space between points is determined by the magnification of the image of

the illuminated sample on the entrance slit of the spectrometer. Submicron
point spacing is easily achieved.

Figure 1.
Schematic illustration of the inside of the spectrometer as set up for spatially resolved
photoluminescence. The dashed lines indicate the path of the light through the spectrometer.

Photoluminescence Setup

Ar laser

cylindrical lens

spherical lenses

512x512 CCD array

output

SPEX spectrometer

input

Computer control: customized software

sample

spherical imaging lenses (25x mag)

Figure 2.
Schematic diagram of spatially resolved photoluminescence system.

System Description

A schematic illustration of the inside of the spectrometer as set up for use in the spatially resolved PL system is shown in Fig. 1. Because the spectrometer grating disperses light only in the direction perpendicular to the entrance slit, spatial information in the direction parallel to the entrance slit is retained. By placing a square CCD array at the output slit, we get an image with wavelength along the horizontal axis and spatial position along the vertical axis. In different language, each row of pixels on the CCD array corresponds to the photoluminescence spectrum associated with a narrow region on the entrance slit. The correspondence between the size of a region on the entrance slit and the size of the sampled region on the semiconductor is determined by the magnification of the imaging optics. We have sampled regions as small as a few microns wide by one micron high. Smaller sampling regions are possible, requiring only larger magnification imaging optics and longer signal integration times to get an adequate signal-to-noise ratio. Because we use a two-lens imaging system, getting a larger magnification requires only the replacement of one lens and minimal re-alignment.

Figure 2 shows a schematic of the overall photoluminescence system. The combination of cylindrical and spherical lenses focuses the pump light onto a vertical line on the sample. That line is then imaged onto the entrance slit of the sample. By focussing the pump onto a line instead of a diffuse spot, we achieve sufficient pump intensity without requiring very high total pump power. The pump source is a SpectraPhysics BeamLok 2060 Argon laser running at 488 nm. The laser, which is owned by Prof. Clifford Pollock and was used to pump dual Ti/Sapphire lasers under a different part of this contract, is located in an adjacent laboratory and the light was piped to the PL setup via a multimode fiber.

Custom Controller Software

The spectral coverage of the CCD array in our spectrometer is only about 10nm, so to cover the 100-150nm necessary for a full PL spectrum, we customized the CCD controller software to automatically take sequential spectra. Between exposures, a TTL output on the CCD controller is used to generate pulse trains which are fed to the stepper motor of the spectrometer. The number of and spatial spacing between spectra, amount of spectrometer advance between frames, exposure time, total number of exposures in the spectrum, and postprocessing options are all user selectable.

Postprocessing options include background subtraction, flatfield correction, median filtering, and output compression. Background subtraction is used to eliminate dark signal from the output, and flatfield correction compensates for pixel to pixel variations in sensitivity. Median filtering is a digital filtering method which removes large narrow spikes without affecting features more than a few pixels wide. Median filtering will not alter a sharp one-sided edge at all, but will completely remove spikes one pixel wide, no matter how high. During long exposures, cosmic rays strike some pixels of the CCD, resulting in one-pixel wide spikes in the output. In addition, the first and last pixels in a row on the CCD frequently have spuriously high values. The use of a median filter after the spectrum has been completely collected removes the spurious spikes, but leaves the photoluminescence data intact. Finally, output compression is used to reduce the size of the array containing the final spectrum. The spectra are collected with one data point for each of the 512 columns of the CCD in every 10 nm

window. In our spectrometer, this corresponds to approximately 0.1Å resolution. For room temperature PL spectra, resolution this high is not necessary, so the output compression feature was added to reduce the otherwise large number of points in the output array. The compression is accomplished by simply replacing a user-specified number of sequential points with their average.

Typical parameters for taking a PL spectrum would include about five spectra taken over a range of 10-15 frames with 10nm spectrometer advance per frame, exposure time per frame of about 60-100 seconds, and background subtraction, flatfield correction and median filtering all activated. Output compression by a factor of five leaves resolution to spare. Once all the parameters have been specified, the custom controller software displays a window on the screen for each spectrum and opens the CCD's shutter to begin the exposure. After the shutter closes, the spectrum data are read in and background subtraction and flatfield corrections are performed. The corrected data is appended to the output array and a pulse train is sent to the spectrometer to advance to the next frame position. After all the frames have been collected, the median filter is performed on the output array and the array is compressed.

Initial Results

To begin characterizing the disordering process, we constructed a small test sample. The sample was a 2mm by 2mm piece of the epitaxial material with the photodetector layers grown on it. On top of the semiconductors we grew, by Plasma Enhanced Chemical Vapor Deposition, a few tenths of a micron of silicon dioxide. PL spectra were recorded before and after annealing, using a Rapid Thermal Annealer in the NNF, at 950°C for 3 minutes. The results are shown in figure 3, normalized to each other. The lumpiness of the curves is due to a bug in the PL system which was later corrected. The spectra show two prominent peaks. The larger peak at shorter wavelength, of which only the tail is visible, is from the GaAs cap on the surface. The smaller, longer wavelength peak is from the InGaAs quantum well. We expect this peak to shift to shorter wavelength and broaden significantly after disordering, which it does. This indicates that we successfully effected disordering in this sample.
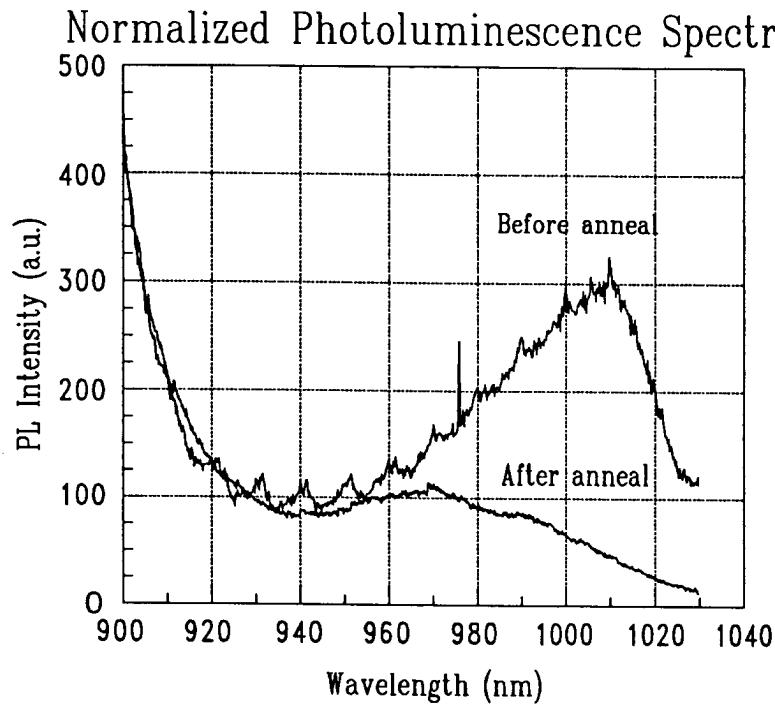
29

Normalized Photoluminescence Spectra

Before anneal

After anneal

Figure 3

Photoluminescence curves of an SiO_2 covered sample before and after a 3 minute 950°C anneal.

Our next step was to test the selectivity against disordering achievable with a silicon nitride barrier layer between the semiconductors and the silicon dioxide. On top of half of a test sample we deposited a 300Å layer of silicon nitride, and on top of the semiconductor and the nitride we deposited a 3000 Å layer of silicon dioxide. The sample structure is depicted in figure 4. PL spectra were taken across the interface. The spectra of this sample before annealing are shown in figure 5. The spectra are virtually identical on both sides of the interface, indicating that the different dielectric layers on top of the two halves of the sample did not have a significant effect on the luminescence. The luminescence intensity is somewhat diminished further from the center because the pump beam is most intense in the center.

Silicon Nitride
300 Angstr.

Silicon Dioxide
3000 Angstr.

GaAs cap

Quantum well
and waveguide layers

GaAs substrate

Figure 4.

Schematic cross-section of the sample used for the disordering characterization in

figures 5 -7

PL Spectra vs. Position
Before annealing

PL Intensity
(Arb. Units)

Wavelength (nm)

Relative Position (100 um)
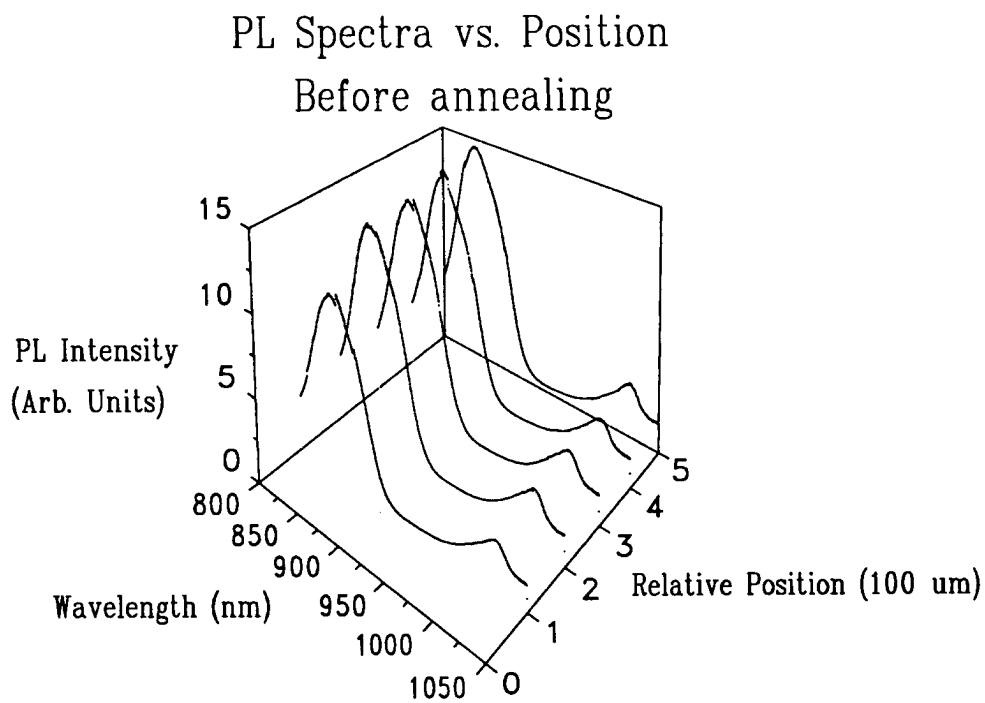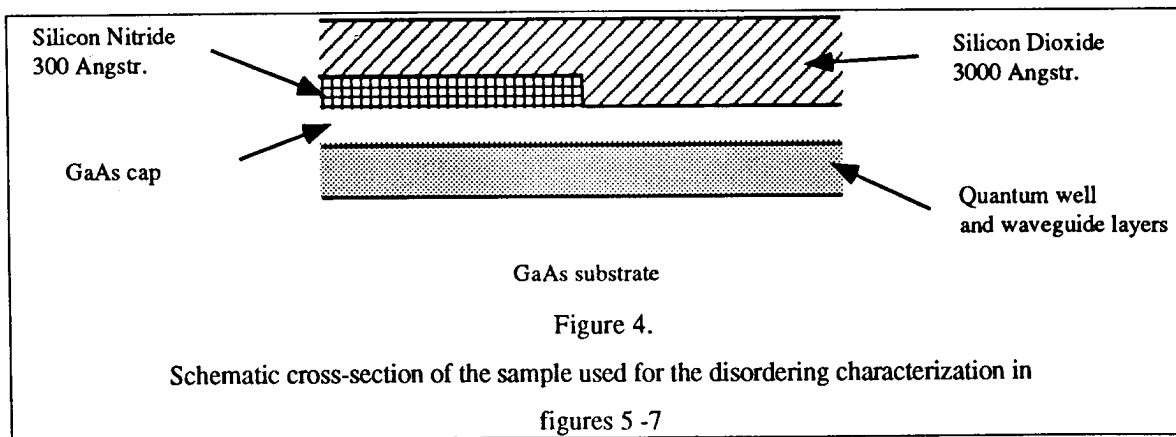
Figure 5.

Spatially resolved photoluminescence curves of a sample half covered with SiN_x and SiO_2 and half covered

with SiO_2. These curves were taken before annealing.

31

After taking the measurement shown in figure 5, the sample was annealed at a temperature of 950°C. We then repeated the photoluminescence spectrum
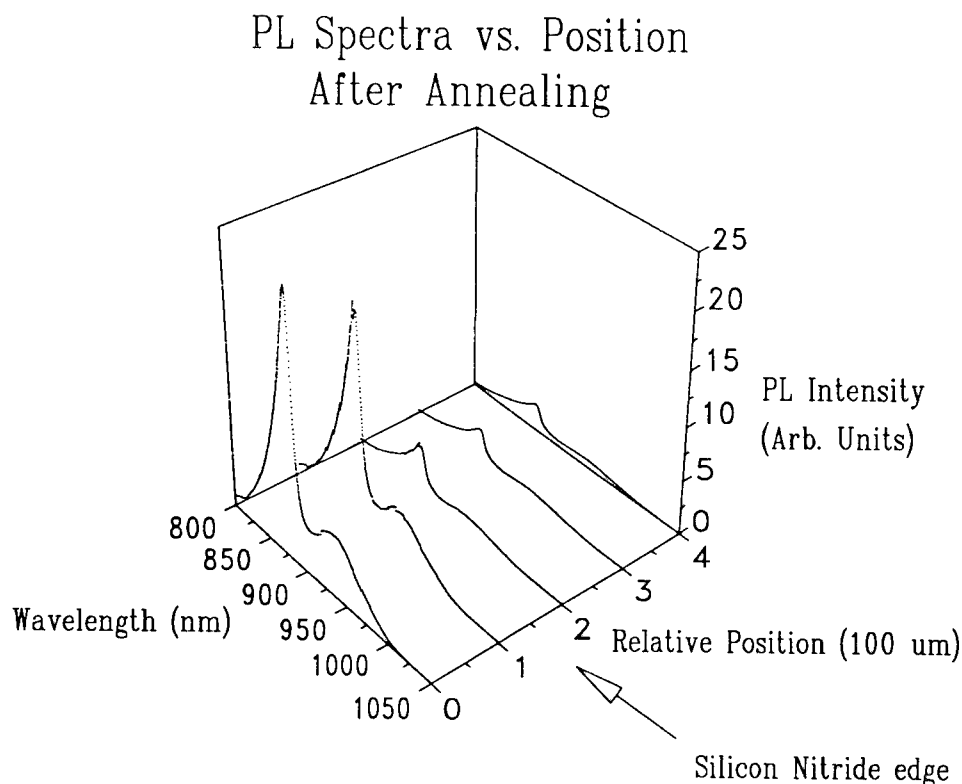
PL Spectra vs. Position
After Annealing

Figure 6.

Spatially resolved PL curves for same sample as Figure 5, but after anneal for 90 seconds at 950°C. The sudden change in the PL intensity occurs at the edge of the SiN$_x$ covered region.

measurement, and obtained the results shown in figure 6. Since the alignment of the PL system was untouched between measurements, and the time between measurements was not more than 20 minutes, changes in PL intensity between figures 5 and 6 are meaningful. The results are rather surprising. The regions covered by only silicon dioxide exhibited disordering as expected, but the regions covered with silicon nitride and silicon dioxide exhibited PL spectra virtually identical in shape to the oxide-only regions. Figure 7 shows a comparison of the PL spectra before and after the anneal. It

is surprising that not only did the silicon nitride appear to not protect against disordering at all, but also the intensity of the luminescence is significantly reduced in the nitride covered regions. Another graduate student at Cornell, Gregory Redinbo from the Materials Science and Engineering department, is also using silicon nitride films identical to ours to protect against disordering. He has done measurements which show that a sample covered with only silicon nitride, annealed at temperatures up to 950°C for times up to one minute, exhibit only slight broadening of the PL peaks from GaAs/AlGaAs quantum wells. The failure of the nitride to protect against disordering in our samples could be related to thermal strain induced by the thick silicon dioxide layer, or could be related to defects in the silicon nitride film. We plan to investigate this further, since this problem is the only remaining barrier to the fabrication of the detectors.

Typical PL Spectra
Before and After Anneal

Before Anneal

After Anneal
Covered with SiO2 only

After Anneal
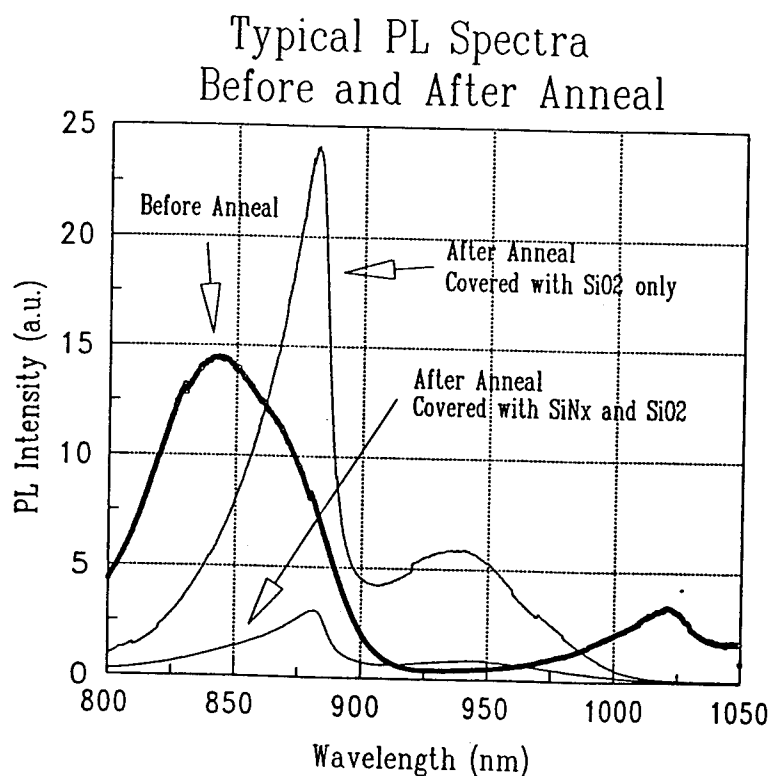Covered with SiNx and SiO2

PL Intensity (a.u.)

Wavelength (nm)

Figure 7.

Comparison of typical PL spectra for unannealed sample and for annealed regions with different encapsulations.

III. PROCESS DEVELOPMENT

Selective Etch Recipe

The major accomplishment in process development this year was a very successful recipe for etching GaAs selectively over AlGaAs in the Reactive Ion Etching system. This etch is used to define the 0.1 mm thick waveguide ridge and stop at a 100Å AlGaAs layer. Our requirements for the etch were good selectivity between AlGaAs and GaAs and also between the SiO_2 mask and GaAs, controllable etch rate, and the absence of unremovable residue on the AlGaAs surface. In the past, chlorofluorocarbon mixtures have been used for this purpose, and give excellent selectivity. However, discharge of CFC's

Average Step Height vs. Etch Time

AlGaAs interface

40 Angstr./sec
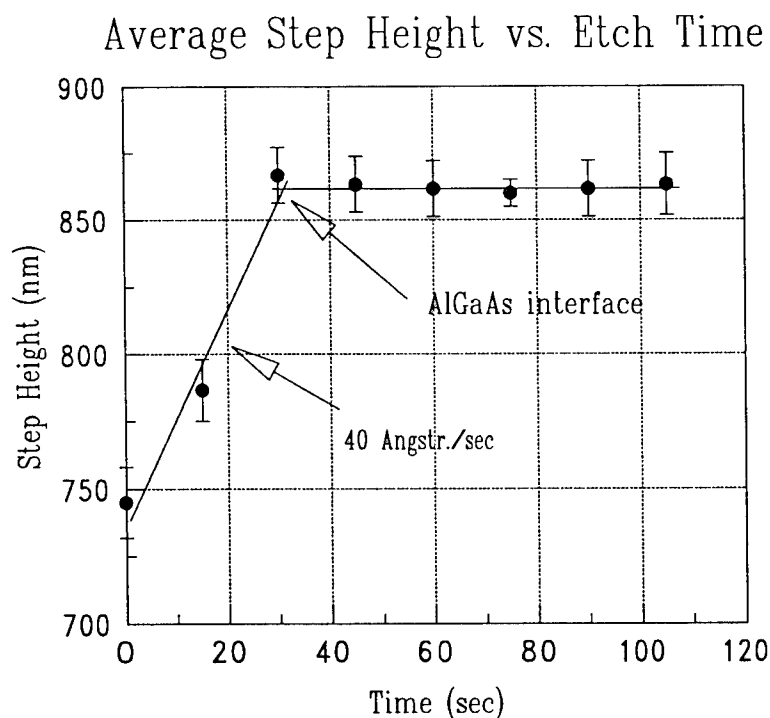
Step Height (nm)

Time (sec)

Figure 8.

Plot of average step height at the edge of an SiO_2 mask vs etching time for a selective GaAs over AlGaAs etch. Sample had a top layer of GaAs on top of an AlGaAs layer.

is now restricted, and the etches tended to leave chemically inert polymers on the AlGaAs surface. The selectivity of the etches is caused by AlF forming on the AlGaAs, so we developed a CFC-free etch by introducing a fluorine containing gas to a standard GaAs etch recipe. Our final recipe is 40 sccm BCl_3, 40 sccm Ar, 4 sccm SF_6, chamber pressure of 20 mtorr, 100V DC self-bias, and 25 watts total RF power. These parameters give a GaAs etch rate of 40 Å/sec, and stops completely on AlGaAs. It also has negligible etch rate of the SiO_2 mask. The graph shown in figure 8 was generated by measuring the etch depth as a function of time. The etch rate can be controlled by varying the etch pressure and RF power, however, increasing the RF power can also decrease the selectivity. We tested for unremovable residue by placing the sample in HCl. Etch depth measurements showed slow but steady etching into the AlGaAs, indicating that no fluorinated polymer residue was left behind by the etch.

Metal Liftoff

In the original process conception we envisioned using the SiO_2 ridge etch mask as a liftoff mask to isolate the gold contacts on either side of the ridge from each other. The SiO_2 was to be etched with buffered HF, which does not attack gold. However, we found that the buffered HF does attack the Ti/Pt adhesion layer between the gold and the semiconductor. The result was that the gold peeled off the surface over a region extending several microns from the base of the ridge. Since the detectors are designed to have a carrier transit distance of 0.9 mm, this is unacceptable.

We solved this problem by replacing the liftoff with a brief gold etch. Since the SiO_2 mask has tall, straight sidewalls, only a small amount of gold adheres to the walls. A brief gold etch removes the metal on the sidewalls but leaves most of the metal on horizontal surfaces behind. The result is that the contacts are electrically isolated from each other, and the SiO_2 etch mask remains on the sample. The presence of the SiO_2 on top of the ridge should not significantly affect the performance of the detectors.

Conclusions

Over the course of this project, we have designed a very efficient 50GHz waveguide photodetector, developed a fabrication process for the detectors, and built a spatially-resolved photoluminescence characterization setup.

Although all of the original contract goals have not been completed, we remain enthusiastic about the feasibility and value of these photodetectors. The basic design remains excellent for monolithic integration in OEIC's. The process development was slowed by myriad minor difficulties which are inevitable when developing a new, innovative process, but no insurmountable problems have arisen. Completion of the characterization of the disordering step is the final step in the process development. After that characterization is complete and suitable annealing parameters are determined, the detectors could be fabricated.

Appendix A
Publications, Presentations, and Dissertations

Publications and Presentations from 1991 - 1994 - Part I

High-Speed Photodetectors for Millimeter Waves", L.F. Eastman, K. Litvin, J. Burm, *GOMAC-91 (Goverment Microcircuit Applications Conference)* , Orlando, FL, (Nov. 4-7, 1991) .

"High Speed Optoelectronics", L.F. Eastman, *1991 Int. Semiconductor Dev. Res. Symp.* Charlotteville, VA, (Dec. 4-6, 1991).

"High Frequency Optical Receivers", L. F. Eastman, K. Litvin J. Burm, D.W. Woodard and W.J. Schaff, *2nd Annual DARPA/Rome Lab. Symp. on Photonics Systems for Antenna Applications (PSSA)*, Monterey, CA (Dec. 10-12, 1991).

"Effects of Quantum Well Design on the Optical and Microwave Performance of Strained Layer InGaAs/GaAs Lasers", S.S. O'Keefe, L.F. Lester, D. Tang, W.J. Schaff and L.F. Eastman, *SPIE - Optoelectronic and Signal Processing for Phased Array Antennas III*, Orlando, FL, (April 20-24, 1992). Proc SPIE -Int. Society of Optical Engineers **1703**, pp. 294-303

"High-Speed Photodetectors for Millimeter Waves", J. Burm, K. Litvin, D. Woodard, W. Schaff and L. Eastman, *SPIE - Optoelectronic Signal Processing for Phased Array Antennas III*, Orlando, FL, (April 20-24, 1992). Proc SPIE-Int. Society of Optical Engineers, **1703**, pp 313-320.

"High Speed/High Frequency Optoelectronic Devices", L.F. Eastman, Invited, *Raytheon*, Lexington, MA (May 15, 1992).

"Compound Semiconductor Materials and Devices Research at Cornell University", L.F. Eastman, P. Mandeville and S. O'Keefe, *Alcatel Alsthom Recherche*, Marcoussis, France, (May 21, 1992). (Vu foils only)

"Compound Semiconductor Materials and Devices Research at Cornell University", L.F. Eastman, P. Mandeville and S. O'Keefe, *Thomson CSF*, Orsay, Cedex, France, (May 22, 1992). (Vu-Foils Only)

"High Frequency Photodiodes for Monolithic Optical Receiver Circuits", K. Litvin, J. Burm, D.W. Woodard, W.J. Schaff, and L.F. Eastman, *WOCSDICE'92* , San Rafael, Spain (May 25-28, 1992).

"High Speed/High Frequency Lasers and PhotoDetectors and Their Optical-Electronic Integrated Circuits", L.F. Eastman, *VII Congresso da Sociedade Brasileira de Microelectrônica*, São Paulo, Brazil, (July 8-10, 1992). (Tutorial also).

"High Frequency Photodiodes for Monolithic Optical Receiver Circuits", K. Litvin, J. Burm, D.W. Woodard, W.J. Schaff and L.F. Eastman, *Engineering Foundation Conf. on 'High Speed Optoelectronic Devices and Circuits II'*, Banff, Alberta, Canada, (Aug. 9-13, 1992).

"Compound Semiconductor Materials and Devices for High Speed/High Frequency Operation", L.F. Eastman, (Invited) *Northwestern University* (Sept. 16, 1992).(Vu-Foils)

"High Speed Optical Devices and Their Integration with Transistors", L. F. Eastman, *SPIE Interational Synposium on Optoelectronic Packaging and Interconnects*, Los Angeles, CA Jan. 18-22, 1993. Proc. ????

"High Speed Microwave and Optoelectronic Devices", L. F. Eastman (Invited) 1993 Princeton Section Sarnoff Symposium (March 26, 1993).

"High Speed/High Frequency Semiconductor Devices" L.F. Eastman, Workshop on Future Trends of Quantum Structures and Device applications", Northwestern Univ., Evanston IL, (June 7-8, 1993).

"High Speed Optical Detectors for Monolithic Millimeter Wave Integrated Circuits", K. Litvin, J. Burm, D. W. Woodard, W Schaff, and L.F. Eastman, IEEE Microwave and Millimeter-Wave Monolithic Circuits Symposium, Atlanta, Ga (June 14-18, 1993).Symposium Digest, (Waymond R. Scott, Jr., Publications Chairman) 1063-1066.

"High Speed Optical Detectors for Monolithic MIillimeter Wave Integrated Circuits", K. Litvin, J. Burm, D. Woodard, W. Schaff, L. F. Eastman, 14th Biennial IEEE/Cornell Conference on "Advanced Concepts in High Speed Semiconductor Devices and Circuits, Aug. 2-4, 1993; Proc. Sec. III-5, pp. 131-140 (1993).

"High Speed Optical Detectors for Monolithic Millimeter Wave Integrated Circuits", Kerry I. Litvin, report for Summer Research Extension Program, RL, Griffiss AFB (Sept. 1993)

"High Speed Optical Detectors for Monolithic Millimeter Wave Integrated Circuits", Kerry Litvin, NNF Annual Industrial Affiliates Meeting (Oct. 26-27, 1993).

"Optimization of High-Speed, High-Frequency MSM Photodetectors", J. Burm, K.I. Litvin, W.J. Schaff and L.F. Eastman, 1993 Int. Semiconductor Device Research Symp., Charlottesville, Va (Dec. 1-3, 1993), Proceedings Engineering Academic Outreach, Univ. VA 1993 749-752.

"High Speed Optical Detectors for Monolithic Millimeter Wave Integrated Circuits" J. Burm, K.I. Litvin, D.W. Woodard, W.J. Schaff and L.F. Eastman, *SPIE's Int. Symp. on Optoelectronic and Microwave Engineering Optoelectronic Signal Processing for Phased Array Antennas IV* , Los Angles, CA (1/22-28/94). Vol. **2155** pages 67-75 (Brian M. Hendrickson-Editor - Soc. Optical Engineering

"High Speed/High Frequency Lasers and MSM Photodetectors", L. F. Eastman, UC/San Diego, April 4, 1994. (Vu-Foils only)

"High Frequency Transistor Research at Cornell", L. F. Eastman, Hughes Research, April 5, 1994. (Vu-Foils only)

"Optoelectronic Devices for High Frequency Operation", L.F. Eastman (Invited) *Fourth Annual 1994 IEEE Mohawk Valley Section Dual-Use Technologies & Applications Conference*, SUNY Inst of Technology at Utica/Rome, NY (May 23-26, 1994).

"Optimized M-S-M Photodetectors", L.F. Eastman, J. Burm, K. Litvin, and W.J. Schaff, *WOCSDICE'94*, Cork, Ireland (May 29-June 2, 1994).

"Optimization of High-Speed Metal-Semiconductor-Metal Photodetectors", J. Burm, K.I. Litvin, W.J. Schaff, and L.F. Eastman, IEEE Photonics Tech. Lett. **6** 722-724 (June 1994).

"Metal-Semiconductor-Metal Photodiodes with Applications in Monolithic Integrated Optical Receiver Circuits Capable of Detecting and Amplifying a Millimeter-Wave Modulation Signal being Transmitted Via an Optical Carrier", K. Litiven, Dissertation Cornell University, (August 1994)

Rome Laboratory

Customer Satisfaction Survey

RL-TR-_____

Please complete this survey, and mail to RL/IMPS,
26 Electronic Pky, Griffiss AFB NY 13441-4514. Your assessment and
feedback regarding this technical report will allow Rome Laboratory
to have a vehicle to continuously improve our methods of research,
publication, and customer satisfaction. Your assistance is greatly
appreciated.
Thank You

_____

_____

Organization Name:_____(Optional)

Organization POC: _____(Optional)

Address:_____

1.   On a scale of 1 to 5 how would you rate the technology
developed under this research?

      5-Extremely Useful   1-Not Useful/Wasteful

                     Rating_____

Please use the space below to comment on your rating.   Please
suggest improvements. Use the back of this sheet if necessary.

2. Do any specific areas of the report stand out as exceptional?

                  Yes____ No_____

     If yes, please identify the area(s), and comment on what
aspects make them "stand out."

3. Do any specific areas of the report stand out as inferior?

<div align="center">Yes_____   No_____</div>

    If yes, please identify the area(s), and comment on what aspects make them "stand out."

4. Please utilize the space below to comment on any other aspects of the report. Comments on both technical content and reporting format are desired.

MISSION

OF

ROME LABORATORY

Mission. The mission of Rome Laboratory is to advance the science and technologies of command, control, communications and intelligence and to transition them into systems to meet customer needs. To achieve this, Rome Lab:

   a. Conducts vigorous research, development and test programs in all applicable technologies;

   b. Transitions technology to current and future systems to improve operational capability, readiness, and supportability;

   c. Provides a full range of technical support to Air Force Materiel Command product centers and other Air Force organizations;

   d. Promotes transfer of technology to the private sector;

   e. Maintains leading edge technological expertise in the areas of surveillance, communications, command and control, intelligence, reliability science, electro-magnetic technology, photonics, signal processing, and computational science.

The thrust areas of technical competence include: Surveillance, Communications, Command and Control, Intelligence, Signal Processing, Computer Science and Technology, Electromagnetic Technology, Photonics and Reliability Sciences.